INTERNATIONAL JOURNAL FOR NUMERICAL METHODS IN FLUIDS
*Int. J. Numer. Meth. Fluids* **28**: 501–521 (1998)

# AN IMPROVED PROJECTION SCHEME APPLIED TO PSEUDOSPECTRAL METHODS FOR THE INCOMPRESSIBLE NAVIER–STOKES EQUATIONS

SANDRINE HUGUES AND ANTHONY RANDRIAMAMPIANINA*

*Institut de Recherche sur les Phénomènes Hors Equilibre, UMR CNRS 6594, Département Modélisation Numérique,*
*La Jetée-Technopôle de Château-Gombert, 38, rue F. Joliot Curie, 13451 Marseille Cedex 20, France*

## SUMMARY

An improved projection scheme is proposed and applied to pseudospectral collocation-Chebyshev approximation for the incompressible Navier–Stokes equations. It consists of introducing a correct predictor for the pressure, one which is consistent with a divergence-free velocity field at each time step. The main objective is to allow a time variation of the pressure gradient at boundaries. From different test problems, it is shown that this method, associated with a multistep second-order time scheme, provides a time accuracy of the same order as the temporal scheme used for the pressure, and also improves the prediction of the velocity slip. Moreover, it does not exhibit any numerical boundary layer mentioned as a drawback of fractional steps algorithm, and does not require the use of staggered grids for the velocity and the pressure. Its effectiveness is validated by comparison with a previous time-splitting algorithm proposed by Goda (K. Goda, *J. Comput. Phys.*, **30**, 76–95 (1979)) and implemented by Gresho (P. Gresho, *Int. j. numer. methods fluids*, **11**, 587–620 (1990)) to finite element approximations. Steady and unsteady solutions for the regularized driven cavity and the rotating cavity submitted to throughflow are also used to assess the efficiency of this algorithm. © 1998 John Wiley & Sons, Ltd.

KEY WORDS: projection scheme; Navier–Stokes equations; pseudospectral Chebyshev methods; unsteady flows

## 1. INTRODUCTION

The objective of this study is to develop an efficient numerical method, which possesses a good temporal behavior for sufficiently large time integration in view of simulations of three-dimensional unsteady flows. For this purpose, a high-order splitting algorithm is developed with a second-order multistep time scheme in the framework of pseudospectral collocation Chebyshev approximations. As well as their high precision, the motivation for the use of spectral methods stems from their very low phase errors for the prediction of time-dependent flow regimes [1,2]. The present article is concerned with the assessment of the effectiveness of the method, particularly its temporal behavior, by validation with analytical solutions and available solutions for the regularized driven cavity and for rotating cavities submitted to superimposed radial throughflow.

---

* Correspondence to: Institut de Recherche sur les Phénomènes Hors Equilibre, UMR CNRS 6594, Département Modélisation Numérique, La Jetée-Technopôle de Château-Gombert, 38, rue F. Joliot Curie, 13451 Marseille Cedex 20, France. Tel.: + 33 491118528; Fax.: + 33 491118502; E-mail: randria@mfmbozy.univ-mrs.fr

CCC 0271–2091/98/130501–21$17.50

*Received 26 February 1997*
*Revised 25 September 1997*

One major problem in solving incompressible Navier–Stokes equations comes from the coupling of the pressure with the velocity, to satisfy the incompressibility constraint. Different techniques were proposed in the literature to overcome this difficulty (e.g. Reference [3]). The use of vorticity and streamfunction formulation of the equations avoids this problem. However, although its application to two-dimensional flows is common, its extension to three-dimensional situations, which is our final goal, is not straightforward, particularly in multiply connected domains (see References [4,5]). In view of solving the lack of evolution equation for the pressure in primitive variables formulation, which is known to be the source of difficulty, Chorin [6] introduced a false explicit time derivative for the pressure, in the artificial compressibility methods (similarly to penalty methods). A version for unsteady flows is presented by Peyret and Taylor [7]. However, this method is basically iterative. Two types of approaches have been proposed independently: first, the coupled method, mainly as the influence matrix technique [8] and the Uzawa scheme, and second, the time-splitting method [9,10]. The main drawback of influence matrix techniques comes from the large memory required, which becomes difficult to manage for three-dimensional unsteady flows. On the other hand, in most cases the Uzawa scheme necessitates iterative process for unsteady flows.

Thus, splitting methods or fractional steps have gained a new interest because of their non-iterative nature. Moreover, they do not require any specific memory storage, and are well adapted for the simulation of unsteady flows. They belong to the predictor-corrector algorithms, where the pressure serves to project a predicted velocity field into a divergence-free space. Several variants are now available from the initial techniques proposed by Chorin [9] and Temam [10]. Two main classes can be identified: the first with an explicit treatment of the velocity predicted from the convection terms, followed by an implicit resolution of the corrected velocity from the diffusion terms. The second class consists of implicitly solving the predicted solution from the momentum equations, followed by an explicit correction step for the velocity. The present algorithm belongs to the latter. Issa [11] linearized the convection terms and included its diagonal part with diffusion terms to implicitly solve the prediction step and explicitly the successive correction steps (up to three). Kim and Moin [12] proposed a semi-implicit treatment of both steps, using a Crank–Nicolson time scheme on the diffusion terms.

However, the main problem concerns the treatment of the pressure, and the associated boundary conditions. Gresho and Sani [13] gave a comprehensive study of the treatment of the pressure boundary conditions necessary to enforce the incompressibility constraint. They showed that only Neumann boundary conditions are appropriate, i.e. they provide a unique solution. Recently, Timmermans *et al.* [14] proposed an approximate projection method, in which Dirichlet boundary conditions are derived for the pressure from the prediction step. On the other hand, Ku *et al.* [15] developed a method which avoids the need to specify boundary conditions for the intermediate predicted velocity field and the pressure, by introducing an algebraic system of equations from the values of the pressure at collocation points and applying the continuity equation at boundaries. Goda [16] proposed an algorithm which differs from these by introducing an intermediate variable proportional to the difference between two successive pressure fields in time, instead of directly solving the pressure itself. Moreover, the pressure gradient obtained at the previous time level is taken into account during the resolution of the predicted velocity (see also Reference [17]). Van Kan [18] has shown that such projection schemes allow the order of accuracy of the temporal scheme used to be kept for the pressure and the velocity. He was the first to report successful application of this algorithm to the prediction of unsteady flows in cavities with source-sink flows, using the finite difference approach associated with a Crank–Nicolson scheme.

Although the use of projection methods is popular with finite difference and volume or finite element approximations, there are only a few applications reported for spectral methods. Orszag and Kells [19] used a tau-Chebyshev–Fourier approximation (with two periodic directions) associated with second-order Crank–Nicolson/Adams–Bashforth schemes for the direct numerical simulation of transition to turbulence in plane Poiseuille and plane Couette flows. Their fractional steps correspond to an explicit evaluation of the predicted velocity and a fully implicit treatment of the correction step. However, Orszag *et al.* [20] mentioned the existence of a numerical divergence boundary layer of thickness $O(\nu\Delta t)^{1/2}$, related to time differencing errors or splitting errors. This is determined directly by the form of the boundary condition to be used for the Poisson equation for the pressure. In a comprehensive theoretical study, these authors have proposed different techniques to circumvent the spurious effects of the splitting errors for the development of high-order methods. Karniadakis *et al.* [21] considered an improved version of the method used by Orszag and Kells [19] and applied it to spectral element methods. Following the theoretical studies of Orszag *et al.* [20], they proposed a higher pressure boundary condition in conjunction with stiffly stable schemes to prevent propagation and accumulation of time differencing errors. The key point of their study resides in the treatment of the Neumann condition used for the Poisson equation. They separated the involved Laplacian of the velocity in the solenoidal part, approximated by an explicit scheme, and in the irrotational part approximated by an implicit scheme. With a spectral tau-Chebyshev approximation, Shen [22] implemented the time-splitting algorithm proposed by Kim and Moin [12] for finite difference methods associated with second-order Crank–Nicolson/Adams–Bashforth schemes. He applied this code to the prediction of the Hopf bifurcation of the unsteady regularized driven cavity flow. However, the pressure is obtained in these cases with an order of accuracy lower than the temporal scheme used. Botella [23] has recently developed a new variant from the former splitting methods of Chorin and Temam, known to be of $O(\Delta t^{1/2})$. He has introduced a temporal scheme of order three, to improve the accuracy of the algorithm and applied it to pseudospectral methods, using different spaces approximation for the velocity and the pressure. Instead of solving a Poisson equation for the pressure, a Darcy problem was used during the projection step, where the pressure is obtained via a 'pseudo-Laplacian' which does not require boundary conditions. The pressure and velocity are obtained with the same order of accuracy as the temporal scheme. On the other hand, Batoul *et al.* [24] have developed a direct solver based on an algorithm named 'projection-diffusion', in which the uncoupling of the velocity and pressure does not necessitate any annex time scheme, as in time-splitting scheme.

In the present paper, an improved time-splitting algorithm, based on the one proposed by Goda [16] and implemented by Gresho [17] to finite element approximations (his 'Projection 2'), is developed for application to pseudospectral Chebyshev methods. The main goal is to solve the main drawback of this former scheme, related to a fixed pressure gradient at boundaries, held at its initial value, during time integration. Indeed, this gradient can vary in actual situations, especially for time-dependent flows and in the presence of forced flows. This is done by introducing a correct predictor for the pressure, derived directly from the Navier–Stokes equations, which provides an appropriate consistent pressure field with a divergence-free velocity. It is also shown that this algorithm allows the order of accuracy of the temporal scheme used to be kept for the pressure and the velocity. The assessment of its efficiency is made by solving the unsteady Navier–Stokes equations in three specific test cases: analytical solutions, the regularized driven cavity and the rotating cavity subject to throughflow. Computed results are compared with available numerical, theoretical and experimental data in the literature for the last two cases.

After the formulation of the problem in Section 2, the solution method is outlined in Section 3, including the spatial approximation with the temporal scheme and emphasis on the projection scheme. Section 4 is devoted to the results obtained for the three specific test cases considered. Section 5 gives the conclusion.

## 2. FORMULATION

Governing equations and numerical methods are presented for two-dimensional situations. Their extension to axisymmetric configurations (for the rotating cavities considered in the paper) is straightforward.

Consider Newtonian incompressible flows, governed by the Navier–Stokes equations:

$$\frac{\partial \mathbf{V}}{\partial t} + \mathbf{V}\cdot\nabla\mathbf{V} = -\nabla p + \frac{1}{Re}\Delta\mathbf{V} + \mathbf{F} \quad \text{in } \Omega,$$

put in the following form:

$$\frac{\partial \mathbf{V}}{\partial t} + N(\mathbf{V}) = -\nabla p + \frac{1}{Re}L(\mathbf{V}) + \mathbf{F} \quad \text{in } \Omega, \tag{1}$$

$$\nabla\cdot\mathbf{V} = 0 \quad \text{in } \Omega, \tag{2}$$

where **V** is the velocity vector, $p$ is the static pressure, **F** a body force, and $Re$ the Reynolds number characteristic of the flow. Specific initial and boundary conditions **W** are given for the velocity field, such that:

$$\mathbf{V} = \mathbf{W} \quad \text{on } \partial\Omega, \quad \text{and} \quad \mathbf{V}^0 = \mathbf{W}^0, \quad \text{at } t = 0, \quad \text{in } \Omega,$$

with

$$\nabla\cdot\mathbf{W}^0 = 0 \quad \text{in } \Omega.$$

A Poisson equation for the pressure is derived from Equations (1) and (2):

$$\Delta p = -\nabla\cdot[N(\mathbf{V}) - \mathbf{F}] \quad \text{in } \Omega. \tag{3}$$

A consistent boundary condition is required to solve this elliptic equation (3), because no natural condition exists. A straight consistent Neumann condition (see Reference [13]) can be derived from Equations (1) and (2):

$$\frac{\partial p}{\partial n} = \mathbf{n}\cdot\left[-\frac{\partial \mathbf{V}}{\partial t} - N(\mathbf{V}) + \frac{1}{Re}L(\mathbf{V}) + \mathbf{F}\right] \quad \text{on } \partial\Omega. \tag{4}$$

In this condition, Karniadakis *et al.* [21] have separated the diffusion term $L(\mathbf{V})$ in solenoidal part, approximated by an explicit scheme, and in irrotational part approximated by an implicit scheme:

$$L(\mathbf{V}) = \nabla(\nabla\cdot\mathbf{V}) - \nabla\times(\nabla\times\mathbf{V}).$$

They have mentioned that the time accuracy of the global solution is directly dependent on the treatment of these pressure boundary conditions. They have tested different time schemes up to order three, and shown that the time differencing error for the velocity field is one order of magnitude smaller than the corresponding error in the boundary divergence, i.e. the order time treatment of the pressure boundary conditions.

## 3. SOLUTION METHOD

### *3.1. Spatial approximation*

A pseudospectral collocation-Chebyshev method is implemented. Each dependent variable is expanded in the approximation space $P_{NM}$, composed of Chebyshev polynomials, $T_n$ and $T_m$ of degrees less or equal than $N$ and $M$ respectively, in the $x$- and $y$-directions. Thus, for $f=(u, v, p)$:

$$f_{NM}(x, y, t) = \sum_{n=0}^{N} \sum_{m=0}^{M} \hat{f}_{nm}(t) T_n(x) T_m(y). \tag{5}$$

The collocation method consists of exactly satisfying the differential equations at special points, the so-called collocation points [1,2]. The Chebyshev–Gauss–Lobatto collocation points are considered, corresponding to the extrema of the Chebyshev polynomials of highest degrees, say $N$ and $M$: $x_i = \cos(i\pi/N)$ and $y_j = \cos(j\pi/M)$ for $i \in [0, N]$ and $j \in [0, M]$. This distribution gives concentrated grid points towards the boundaries, with the distance between the last collocation point and the boundary of $O(N^{-2})$ for a degree $N$. Thus, the system of equations to be treated is solved directly in the physical space on these collocation points for each variable $f_{NM}(r_i, z_j, t)$ for $i \in [1, N-1]$ and $j \in [1, M-1]$, with associated boundary conditions. But differentiation is accomplished efficiently by means of a transform method, and by using a recurrence relation in spectral space [1,2].

The velocity and the pressure are solved on the same grid $P_{NM} \times P_{NM}$.

### *3.2. Temporal scheme*

The time integration used is second-order-accurate and is based on a combination of Adams–Bashforth and backward differentiation formula (AB/BDF) schemes, chosen for its good stability properties [25]. The resulting scheme AB/BDF is semi-implicit, and for Equation (1), it writes as:

$$\frac{3\mathbf{V}^{n+1} - 4\mathbf{V}^{n} + \mathbf{V}^{n-1}}{2\Delta t} + 2N(\mathbf{V}^{n}) - N(\mathbf{V}^{n-1}) = -\nabla p^{n+1} + \frac{1}{Re}\Delta \mathbf{V}^{n+1} + \mathbf{F}^{n+1}. \tag{6}$$

It belongs to the stiffly stable schemes family [26] also used in Karniadakis *et al.* [21]. Then, at each time step, the problem reduces to the resolution of Helmholtz and Poisson equations.

For the initial step, we have taken $V^{-1} = V^{0}$.

On Chebyshev collocation points, these Helmholtz and Poisson equations are solved efficiently by using a complete diagonalization of operators in both directions [27,28], as all eigenvalues are real and negative [1,2]. The computation of eigenvalues, eigenvectors and the inversion of the corresponding matrices are done once in a preprocessing step before starting the time integration. Thus, at each time iteration, the solution is obtained from simple matrices products.

### *3.3. The improved projection scheme (IPS)*

The improved projection scheme corresponds to a modified version of the one proposed by Goda [16], and implemented by Gresho [17] ('Projection 2') to finite element methods.

In the version (hereafter referred to as PSG) reported by these authors, the first step implicitly solves a predicted velocity from the momentum equation, taking into account the pressure gradient obtained from previous time level. This leads to a fixed normal pressure gradient during the time integration, held at its initial value (see Reference [17]). The purpose of the present projection scheme is to solve this drawback, by introducing a preliminary pressure at each time step, which allows a variation in time of the normal pressure gradient at boundaries. This predictor also maintains the order accuracy of the temporal scheme used for the global solution. Moreover, it will be shown later that this pressure step improves the prediction of the velocity slip.

The fractional steps proceed as follows.

(i) The predictor for the pressure: before each time iteration, solve for the preliminary pressure $\bar{p}^{n+1}$ from Navier–Stokes and continuity equations:

$$\Delta\bar{p}^{n+1} = \nabla\cdot[-2N(\mathbf{V}^n) + N(\mathbf{V}^{n-1}) + \mathbf{F}^{n+1}] \quad \text{in } \Omega, \tag{7}$$

with

$$\frac{\partial\bar{p}^{n+1}}{\partial n} = \mathbf{n}\cdot\left\{\frac{-3\mathbf{W}^{n+1} + 4\mathbf{V}^n - \mathbf{V}^{n-1}}{2\Delta t} - 2N(\mathbf{V}^n) + N(\mathbf{V}^{n-1}) + \frac{1}{Re}[2L(\mathbf{V}^n) - L(\mathbf{V}^{n-1})] + \mathbf{F}^{n+1}\right\} \quad \text{on } \partial\Omega. \tag{8}$$

(ii) Solve implicitly for a predictor $\mathbf{V}^*$ for the velocity from the momentum equation, including this pressure field:

$$\frac{3\mathbf{V}^* - 4\mathbf{V}^n + \mathbf{V}^{n-1}}{2\Delta t} + 2N(\mathbf{V}^n) - N(\mathbf{V}^{n-1}) = -\nabla\bar{p}^{n+1} + \frac{1}{Re}\Delta\mathbf{V}^* + \mathbf{F}^{n+1} \quad \text{in } \Omega, \tag{9}$$

with the actual boundary conditions

$$\mathbf{V}^* = \mathbf{W}^{n+1} \quad \text{on } \partial\Omega. \tag{10}$$

(iii) The correction step consists of the explicit evaluation of the final divergence-free velocity field:

$$\frac{3\mathbf{V}^{n+1} - 3\mathbf{V}^*}{2\Delta t} = -\nabla(p^{n+1} - \bar{p}^{n+1}) \quad \text{in } \bar{\Omega} = \Omega\bigcup\partial\Omega, \tag{11}$$

and

$$\nabla\cdot\mathbf{V}^{n+1} = 0 \quad \text{in } \Omega, \tag{12}$$

with $\mathbf{n}\cdot\mathbf{V}^{n+1} = \mathbf{n}\cdot\mathbf{W}^{n+1} = \mathbf{n}\cdot\mathbf{V}^*$ on $\partial\Omega$.

The latter step is solved through an intermediate variable $\phi$, defined as $\phi = 2\Delta t/3(p^{n+1} - \bar{p}^{n+1})$. Taking the divergence of Equation (11) with (12) yields a Poisson equation for $\phi$:

$$\Delta\phi = \nabla\cdot\mathbf{V}^* \quad \text{in } \Omega, \tag{13}$$

with the consistent Neumann boundary condition (see References [13] and [17]):

$$\frac{\partial\phi}{\partial n} = 0 \quad \text{on } \partial\Omega. \tag{14}$$

Finally, update the corrected pressure and velocity fields in $\bar{\Omega} = \Omega\cup\partial\Omega$:

$$p^{n+1} = \bar{p}^{n+1} + \frac{3}{2\Delta t}\phi,$$

$$\mathbf{V}^{n+1} = \mathbf{V}^* - \nabla\phi.$$

*3.3.1. Remarks.* In the PSG version, the prediction step for the pressure is carried out once at the start of the problem to provide an appropriate pressure field, and thus $\bar{p}^{n+1}$ is to be replaced by $p^n$ in the different fractional steps. For the present scheme, it is clearly shown from Equation (14) and the definition of the variable $\phi$, that the normal pressure gradient at boundaries is allowed to vary during time integration:

$$\frac{\partial\phi}{\partial n} = 0 \Rightarrow \frac{\partial\bar{p}^{n+1}}{\partial n} = \frac{\partial p^{n+1}}{\partial n} \neq \frac{\partial p^n}{\partial n} \quad \text{on } \partial\Omega,$$

while in the PSG:

$$\frac{\partial\phi}{\partial n} = 0 \Rightarrow \frac{\partial p^{n+1}}{\partial n} = \frac{\partial p^n}{\partial n} = \cdots = \frac{\partial p^0}{\partial n},$$

on $\partial\Omega$ at each time step, as in this case:

$$\phi = \frac{2\Delta t}{3}(p^{n+1} - p^n).$$

$\mathbf{V}$ slips on $\partial\Omega$, since boundary conditions on the normal component only are enforced to have a well-posed problem. Gresho [17] has shown that for the PSG method:

$$\tau \cdot (\mathbf{V} - \mathbf{W}) = -\tau \cdot \nabla\phi = -\frac{2\Delta t^2}{3}\frac{\partial\dot{p}}{\partial\tau} + O(\Delta t^3), \tag{15}$$

with the simple approximation $\dot{p} = [p^{n+1} - p^n]/\Delta t$. In a similar way, for the IPS method, we have:

$$\tau \cdot (\mathbf{V} - \mathbf{W}) = -\tau \cdot \nabla\phi = -\frac{2\Delta t^2}{3}\left(\frac{\partial\dot{P}}{\partial\tau}\right) + O(\Delta t^3),$$

where $\dot{P} = (p^{n+1} - \bar{p}^{n+1})/\Delta t$.

In the boundary conditions imposed for the pressure field $\bar{p}$, a second-order Adams–Bashforth scheme is used for the diffusion term $L(\mathbf{V})$ expressed in the form proposed by Karniadakis *et al.* [21] (see also Reference [7]), to improve the stability of the solution:

$$L(\mathbf{V}) = -\nabla \times (\nabla \times \mathbf{V}).$$

The present scheme differs from the one proposed by Timmermans *et al.* [14] by the treatment of this predictor for the pressure and also on the definition of the intermediate variable $\phi$. They have introduced a predictor for the pressure with an $O(\Delta t)$ while using a temporal scheme of $O(\Delta t^2)$.

## 4. RESULTS

Three test problems consisting of the resolution of time-dependent Navier–Stokes equations have been considered to assess the effectiveness of the new algorithm (IPS). The first case will serve to show the temporal behavior of the IPS method in comparison with the former PSG method on the computed solution. Then the IPS method will be applied to the two following test problems, and results will be compared with available solutions in the literature.

Firstly, exact solutions are constructed from the Navier–Stokes equations by introducing analytical source terms **F**.

Secondly, steady and unsteady flows inside the regularized square driven cavity are considered. The results are validated by comparisons with available numerical solutions also obtained with spectral Chebyshev approximations but using different approaches: in primitive variables formulation with other time-splitting methods (Shen [22] and Botella [23]) and in vorticity-streamfunction formulation with an influence matrix technique (Ehrenstein [29], Ehrenstein and Peyret [30]).

Finally, the axisymmetric Ekman layer flow regimes developing inside rotating cavities submitted to radial throughflow are treated. The results are compared with available theoretical [32], experimental [33] and numerical [34] solutions. The latter have been obtained with a pseudospectral collocation-Chebyshev method, associated with the same time scheme used here, under vorticity-streamfunction formulation and using an influence matrix technique [35].

### 4.1. Analytical time-dependent NSE solutions

The two algorithms are both implemented to the aforementioned pseudospectral collocation-Chebyshev approximation with the second-order time scheme AB/BDF. Exact solution of the Navier–Stokes equations (1) and (2) is built from analytical source term:

$$\mathbf{F} = \begin{pmatrix} -\dfrac{1}{Re}\left[\beta Re \sin(\beta t) - \dfrac{\pi^2}{2}\cos(\beta t)\right]\sin\left(\dfrac{\pi x}{2}\right)\cos\left(\dfrac{\pi y}{2}\right) + \alpha\cos(\beta t) \\ \dfrac{1}{Re}\left[\beta Re \sin(\beta t) - \dfrac{\pi^2}{2}\cos(\beta t)\right]\cos\left(\dfrac{\pi x}{2}\right)\sin\left(\dfrac{\pi y}{2}\right) + \alpha\cos(\beta t) \end{pmatrix}$$

where $\alpha$ and $\beta$ are two constants.

The exact solution corresponds to:

$$\mathbf{V}(x, y, t) = \begin{pmatrix} \cos(\beta t)\sin\left(\dfrac{\pi x}{2}\right)\cos\left(\dfrac{\pi y}{2}\right) \\ -\cos(\beta t)\cos\left(\dfrac{\pi x}{2}\right)\sin\left(\dfrac{\pi y}{2}\right) \end{pmatrix}$$

and

$$p(x, y, t) = \cos^2(\beta t)[\cos(\pi x) + \cos(\pi y)]/4 + (x + y)\alpha\cos(\beta t).$$

Thus, a value $\alpha \neq 0$ generates variations in time of the normal pressure gradient at boundaries.

For the present test, the following set of parameter values were considered: $Re = 100$, $\beta = 5$ for two values of $\alpha$: 0 (constant pressure gradient at boundaries) and 10, respectively. The spatial resolution is fixed at $N = M = 32$, and $N = M = 40$ in some cases to test the spatial accuracy of the solution.

To measure the temporal accuracy of both methods, the following norm has been considered:

$$E_{\text{tot}}(f) = \max_t \left\{\frac{1}{NM}\sum_{i=0}^{N}\sum_{j=0}^{M}[f(x_i, y_j, t) - f_{NM}(x_i, y_j, t)]^2\right\}^{1/2},$$

where $E_{\text{int}}(f)$ and $E_{\text{bou}}(f)$ correspond to the restriction of $E_{\text{tot}}(f)$ at the interior domain and at boundaries respectively, and $f(x, y, t)$ represents the exact solution. These errors are reported for the velocity component $u$ and for the pressure $p$ during eight periods, $t \in [4\pi/5, 4\pi]$, when the periodic state is well established. $E_{\text{bou}}(u)$ provides an evaluation of the velocity slip.

*4.1.1. Time-splitting errors.* From their definition, the two projection schemes PSG and IPS satisfy exactly the incompressibility constraint inside the interior domain $\Omega$ at each time iteration, irrespective of the time step, the spatial resolution and the flow characteristics. Therefore, the numerical divergence boundary layer mentioned by Orszag *et al.* [20] was not observed during our simulation.

To give an insight on the slip, the values of $E_{\text{bou}}(u)$ are reported in Figure 1. Irrespective of the value of $\alpha$ considered, the IPS method exhibits a temporal behavior of $O(\Delta t^3)$, which indicates that $(\partial \dot{P}/\partial \tau) \sim O(\Delta t)$ at least. For the former PSG method, a variation of $E_{\text{bou}}(u)$ in $O(\Delta t^2)$ is observed, in accordance with Equation (15). Moreover, it is shown that the new algorithm improves the prediction of the slip with an order of magnitude varying from three for the highest time step (close to numerical stability limit) to four at the lowest time step. The saturation solution obtained with the time step $\Delta t = 5 \times 10^{-4}$ shows the spatial accuracy limit for $N = M = 32$. Indeed, with a higher resolution $N = M = 40$, the solution follows again the $O(\Delta t^3)$ behavior.

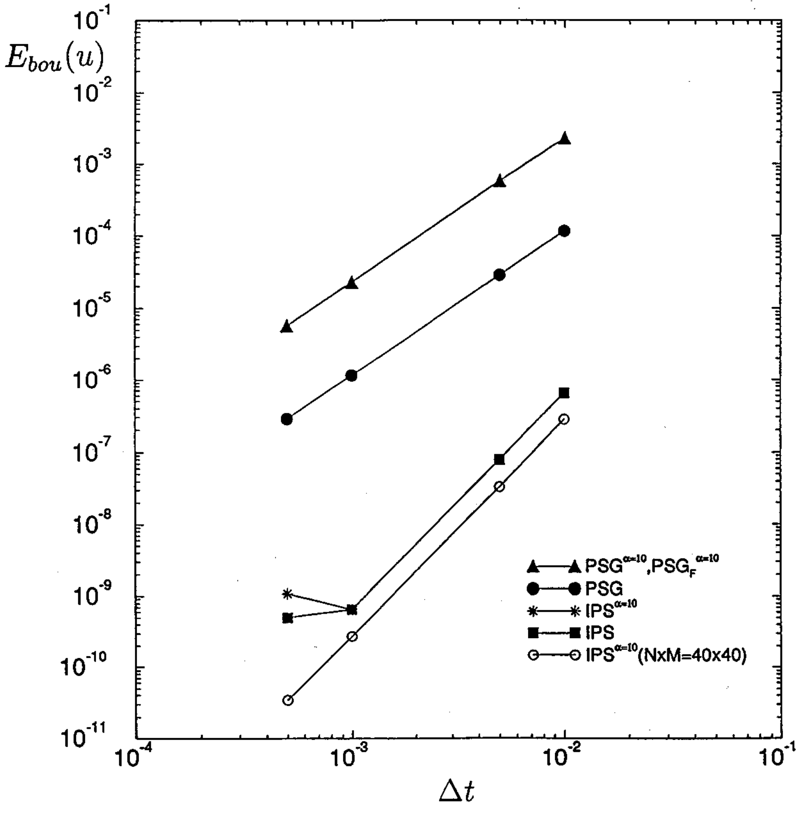

Figure 1. Plot of $L_2$-error of the velocity slip $E_{\text{bou}}(u)$ versus time step $\Delta t$ for the two projection schemes PSG and IPS.

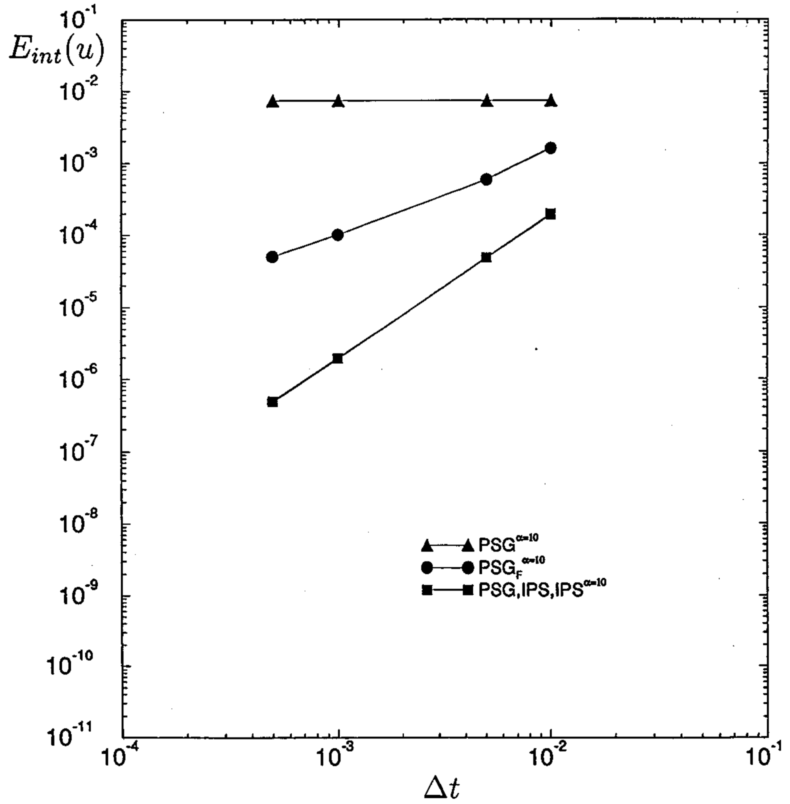

Figure 2. Plot of $L_2$-error $E_{\text{int}}(u)$ of the velocity component $u$ inside the interior domain versus time step $\Delta t$ for the two projection schemes PSG and IPS. Effects of the variation of the normal pressure gradient at boundaries: $\alpha = 0$ and 10.

*4.1.2. Temporal accuracy.* When there is no pressure gradient variations in time at the boundaries, $\alpha = 0$, both methods exhibit the same expected temporal behavior in $O(\Delta t^2)$ for the velocity and for the pressure inside the whole domain (Figures 2 and 3). For the error on the pressure at boundaries, it is noted that it follows the same behavior as the error obtained at the interior domain $E_{\text{int}}(p)$, indicating the important role of pressure boundary conditions on the solution.

When the normal pressure gradient at boundaries is enforced to vary in time, $\alpha = 10$, different behaviors are observed. First, the IPS method (denoted $\text{IPS}^{\alpha=10}$ in the figures) exhibits the expected $O(\Delta t^2)$ behavior for the velocity (Figure 2) and for the pressure (Figure 3). The PSG method, however, presents a saturation of total errors for the two variables, because of the inappropriate treatment of the pressure gradient at boundaries. This is reflected by the variation of the pressure at boundaries (Figure 3). Some computations have been carried out by filtering (setting to 0) the two highest modes in each direction for the pressure, say $\hat{p}_{nm} = 0$ for $n = N$, $N - 1$ and $m = M$, $M - 1$ from Equation (5). Thus, an improvement of the solution is obtained, denoted $PSG_F^{\alpha=10}$ in Figure 3, but with an $O(\Delta t)$. As these highest modes carry the information on the boundary conditions, setting them to 0 has 'removed' the inadequate conditions on the method. The initial pressure field is obtained for the PSG method from the resolution of Equation (7) with (8), in which the initial velocity field corresponds to the exact solution at $t = 0$.

From these results, some first conclusions are drawn:

- From their definition, the two projection schemes do not exhibit any numerical boundary layer divergence induced by splitting errors.
- The PSG method provides the correct behavior when the solution does not present any time variation of the pressure gradient at boundaries, and otherwise shows a saturation of the solution. In this case, filtering of the two highest spectral coefficients of the pressure in the two directions brings an improvement of the solution, but with an $O(\Delta t)$ accuracy, comparatively to the order of the temporal scheme used $O(\Delta t^2)$. This suggests that the observed saturation may result from a 'bad' resolution of these modes, coming from the inadequate boundary conditions of the pressure. However, the reason for the loss of accuracy is not yet clearly understood.
- The predictor for the pressure introduced in the new algorithm IPS brings a solution to these drawbacks mentioned for the former PSG method. This results from a better prediction of the pressure field, consistent with a divergence-free velocity. Moreover, the velocity slip at boundaries is reduced by one order of magnitude compared with the temporal accuracy of the velocity, and comparatively to the former method PSG. The solutions are also independent of the pressure gradient variations at boundaries during time integration.

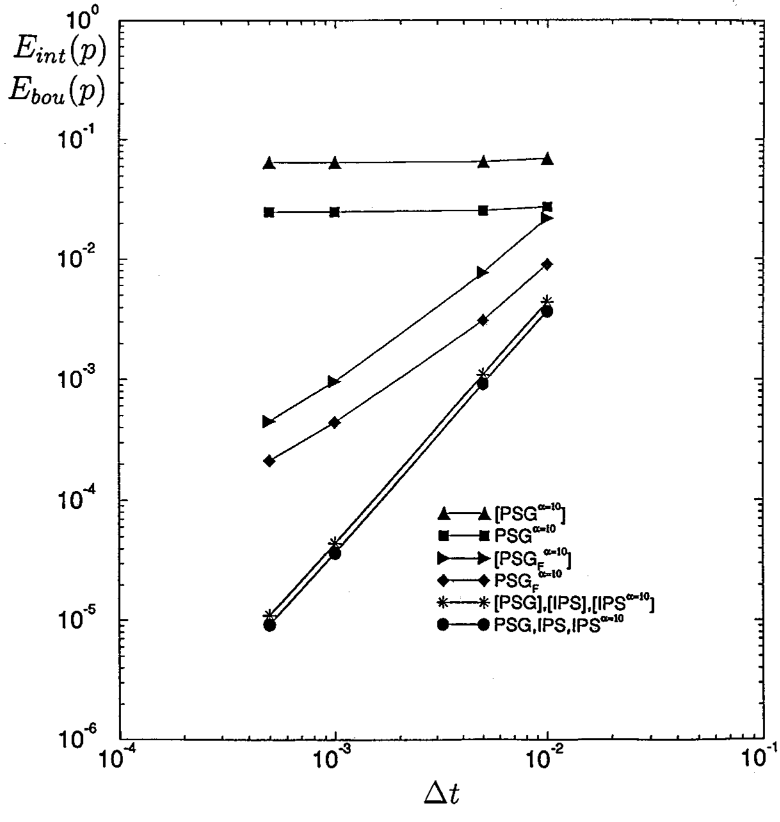

Figure 3. Plot of $L_2$-error $E_{\text{int}}(p)$ and $E_{\text{bou}}(p)$ of the pressure $p$ versus time step $\Delta t$ for the two projection schemes PSG and IPS. Effects of the variation of the normal pressure gradient at boundaries: $\alpha = 0$ and 10. Variables between ▯ correspond to values at boundaries $E_{\text{bou}}(p)$.

Table I. Computational costs in CRAY-c98 CPU seconds and memory requirements in 64-bit words for the resolution of the Navier–Stokes equations

| $N=M$ | Preprocessing | Poisson solver | One iteration | Memory |
|---|---|---|---|---|
| 16 | 1.68522E-02 | 1.39512E-04 | 2.52829E-03 | 343214 |
| 20 | 2.38183E-02 | 2.0397E-04 | 3.33118E-03 | 355742 |
| 24 | 3.272E-02 | 2.8534E-04 | 4.359E-03 | 370958 |
| 32 | 5.4558E-02 | 5.11317E-04 | 6.5469E-03 | 409582 |
| 40 | 8.15224E-02 | 8.6683E-04 | 9.77865E-03 | 459022 |
| 48 | 0.115259 | 1.34985E-03 | 1.3381E-02 | 519374 |

*4.1.3. Computational details.* The computational costs in CRAY c-98 CPU seconds are given for different resolutions in Table I, for the preprocessing step, the resolution of a Poisson equation and one iteration for the IPS method. The preprocessing step corresponds to the computation of the different coefficients used for fast Fourier transforms and derivatives, the eigenvalues, the eingenvectors and the inversion of matrices for the Helmholtz and Poisson equations. As mentioned before, the solution is obtained (during the time iteration) from the products of simple matrices after a complete diagonalization of operators in both directions. One iteration includes the resolution of two Helmholtz ($u$ and $v$) and two Poisson equations ($\bar{p}$ and $\phi$), with the correction step. We recall that the boundary conditions for the predictor of pressure (Equation (8)) must be calculated at each time step, contrary to the other variables. The resolution of the preliminary pressure field $\bar{p}$ does not bring excessive cost, particularly due to the efficient solver used for the Poisson equation. A variation of the CPU time for one iteration in function of the resolution is found to be $5\times 10^{-6}N^2$, which is reasonably good. The memory requirements for different spatial resolutions are also reported in Table I. It follows a variation in $O(N^2)$.

The new method IPS is now applied to the computations of steady and unsteady flows in the regularized driven cavity and the rotating cavity submitted to radial throughflow.

### *4.2. The regularized driven cavity*

The second problem corresponds to the regularized driven cavity, studied by Ehrenstein [29] (see also Reference [30]). The lateral and bottom walls are kept stationary, while the top lid moves with a horizontal velocity component $u(x, 1) = -(1-x^2)^2$ and $v(x, 1) = 0$ for $(x, y)\in[-1, 1]^2$. Shen [22] and Batoul *et al.* [24] have studied the same configuration ,but with the upper wall moving in opposite direction.

*4.2.1. Numerical stability.* The critical time steps for different spatial resolutions are presented in Table II for two values of $Re = 100$ and 400, to allow comparisons with available data in the literature. The good behavior of the method, which for instance at $Re = 400$ follows a variation in $O(1/N)$ as already mentioned in Reference [30] (Table IV) is observed. These authors have used the same temporal scheme associated with the Chebyshev collocation method, as in this paper, but with a vorticity-stream function formulation (thus reducing the number of equations to two, instead of four solved here). The present values are also similar to the results obtained by Botella [23] with his Chebyshev projection scheme using a third-order accuracy in time. Thus, the present algorithm does not bring severe restrictions to

Table II. Values of critical time step $\Delta t_c$ for $Re = 100$ and 400 (with an error $\pm 5 \times 10^{-4}$).

| $N = M$ | $Re = 100$ | $Re = 400$ |
|---|---|---|
| 16 | 0.090 | 0.055 |
| 20 | 0.081 | 0.041 |
| 24 | 0.073 | 0.033 |
| 32 | 0.061 | 0.027 |

the stability properties of the temporal scheme, as its order of accuracy is kept for the pressure and the velocity.

*4.2.2. Steady flows.* Comparisons of some characteristic flow variables are made with previous numerical results obtained by Ehrenstein [29] (Table III) and reported in Reference [30] (Table V) for two values of the Reynolds number, $Re = 100$ and 400.

The comparisons are carried out for different spatial resolutions on the extremum values of the streamfunction $\psi$ with its location (corresponding to the primary vortex) and of the vorticity $\zeta$ at the moving top lid $(x, 1)$:

$M_1 = \max |\psi|$ at collocation points;
$M_2 = \max |\zeta|$ at collocation points; and
$M_3 = \max |\zeta|$ from solution interpolated on $201 \times 201$ uniform grids.

The present results are reported in Tables III and IV.

These comparisons show a good overall agreement, especially on the prediction of the different locations. The present results follow the same behavior of the solution when varying the spatial resolutions. The interpolation to a $201 \times 201$ equidistant mesh provides a good indication of the solution, as the mesh size is close to the distance between the boundary and the nearest collocation point for the largest resolution considered, $N = M = 32$ (it corresponds to the smallest mesh size for the collocation grids). For the lowest value of $Re$ (Table III), our results agree very well with the solutions obtained by Ehrenstein [29] and also reported in Ehrenstein and Peyret [30] for spatial resolutions $N = M > 16$ on the maximum value of the streamfunction, and for $N = M > 20$ on the maximum value of the vorticity at the moving lid. For $Re = 400$ (Table IV), small discrepancies are observed, particularly on the maximum values of the vorticity at the upper moving wall. Nevertheless, the largest difference for the

Table III. Effect of the resolution on characteristic flow variables $M_1$, $M_2$, $M_3$, for the regularized driven cavity: $Re = 100$

| $N = M$ | $M_1$ | $M_2$ | $M_3$ | $M_3^E$ | $M_3^B$ |
|---|---|---|---|---|---|
| 16 | 8.3158E-02<br>(0.40, 0.78) | 13.3604<br>(0.60) | 13.4619<br>(0.62) | 13.4663<br>(0.62) | 13.4476<br>(0.62) |
| 20 | 8.2695E-02<br>(0.42, 0.73) | 13.1774<br>(0.65) | 13.4463<br>(0.62) | 13.4459<br>(0.62) | 13.4441<br>(0.62) |
| 24 | 8.3315E-02<br>(0.37, 075) | 13.4226<br>(0.63) | 13.4447<br>(0.62) | 13.4446<br>(0.62) | 13.4446<br>(0.62) |
| 32 | 8.3402E-02<br>(0.40, 0.74) | 13.3422<br>(0.60) | 13.4447<br>(0.62) | 13.4447<br>(0.62) | 13.4448<br>(0.62) |

Comparison of values of $M_3$ with results obtained in [29,30] ($M_3^E$) and in [23] ($M_3^B$).

Table IV. Effect of the resolution on characteristic flow variables $M_1$, $M_2$, $M_3$ for the regularized driven cavity: $Re = 400$

| $N = M$ | $M_1$ | $M_2$ | $M_3$ | $M_3^E$ | $M_3^B$ |
|---|---|---|---|---|---|
| 16 | 8.5979E-02 | 25.0387 | 25.3854 | 25.4675 | 25.1604 |
| | (0.40, 0.60) | (0.60) | (0.62) | (0.62) | (0.625) |
| 20 | 8.5185E-02 | 24.6404 | 24.9458 | 24.9846 | 24.9273 |
| | (0.42, 0.58) | (0.65) | (0.62) | (0.63) | (0.63) |
| 24 | 8.5718E-02 | 24.9180 | 24.9170 | 24.9333 | 24.9148 |
| | (0.43, 0.63) | (0.63) | (0.63) | (0.63) | (0.63) |
| 32 | 8.5481E-02 | 24.7844 | 24.9107 | 24.9110 | 24.9111 |
| | (0.40, 0.60) | (0.65) | (0.63) | (0.63) | (0.63) |
| 40 | | | | | 24.9109 |
| | | | | | (0.63) |

Comparison of values of $M_3$ with results obtained in [29,30] ($M_3^E$) and in [23] ($M_3^B$).

highest mesh ($N = M = 32$) remains $< 0.02\%$ for all values compared. Comparisons with recent numerical results obtained by Botella [23] with a $O(\Delta t^3)$ time accurate scheme confirm also the good behavior of the present method (see Tables III and IV).

Streamlines with corresponding isobaric lines are displayed in Figure 4 for $Re = 400$ obtained with a resolution of $N = M = 32$. The flow structure is well represented with secondary vortices, compared with available solutions in the literature. There is also good behavior of the isobaric lines structure compared with the isobaric contours reported by Morchoisne [31] for smaller value of $Re$, $Re = 200$.

*4.2.3. Unsteady flows.* Comparisons are carried out with the results obtained by Shen [22] for non-stationary solutions. He obtained steady state solution at value of $Re \leq 10000$. He argued that the effective Reynolds number for the regularized driven cavity should be less than that for the driven cavity (where a constant value of one is imposed everywhere along the upper boundary). He found that the Hopf bifurcation does occur for the range of $Re$ belonging to [10000, 10500]. More recently, Batoul *et al.* [24], applying their 'projection-diffusion' algorithm with pseudospectral Chebyshev methods, gave more precise range for the critical $Re \in [10250, 10300]$. Since our purpose is not to compute the exact threshold of the unsteady

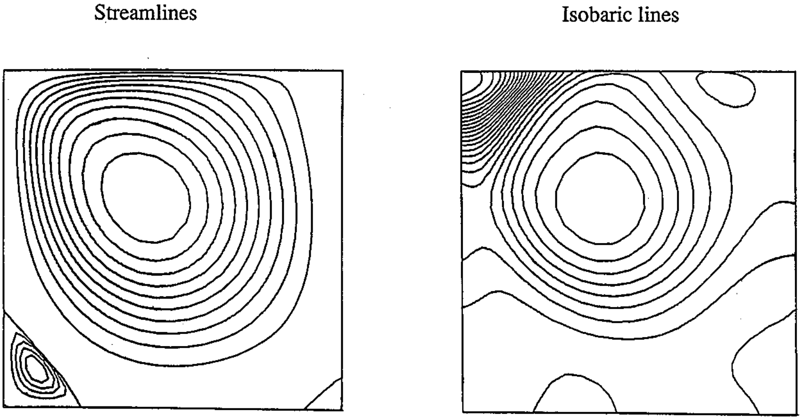

Figure 4. Streamlines and isobaric lines for the regularized driven cavity: steady flow at $Re = 400$, $N \times M = 32 \times 32$.

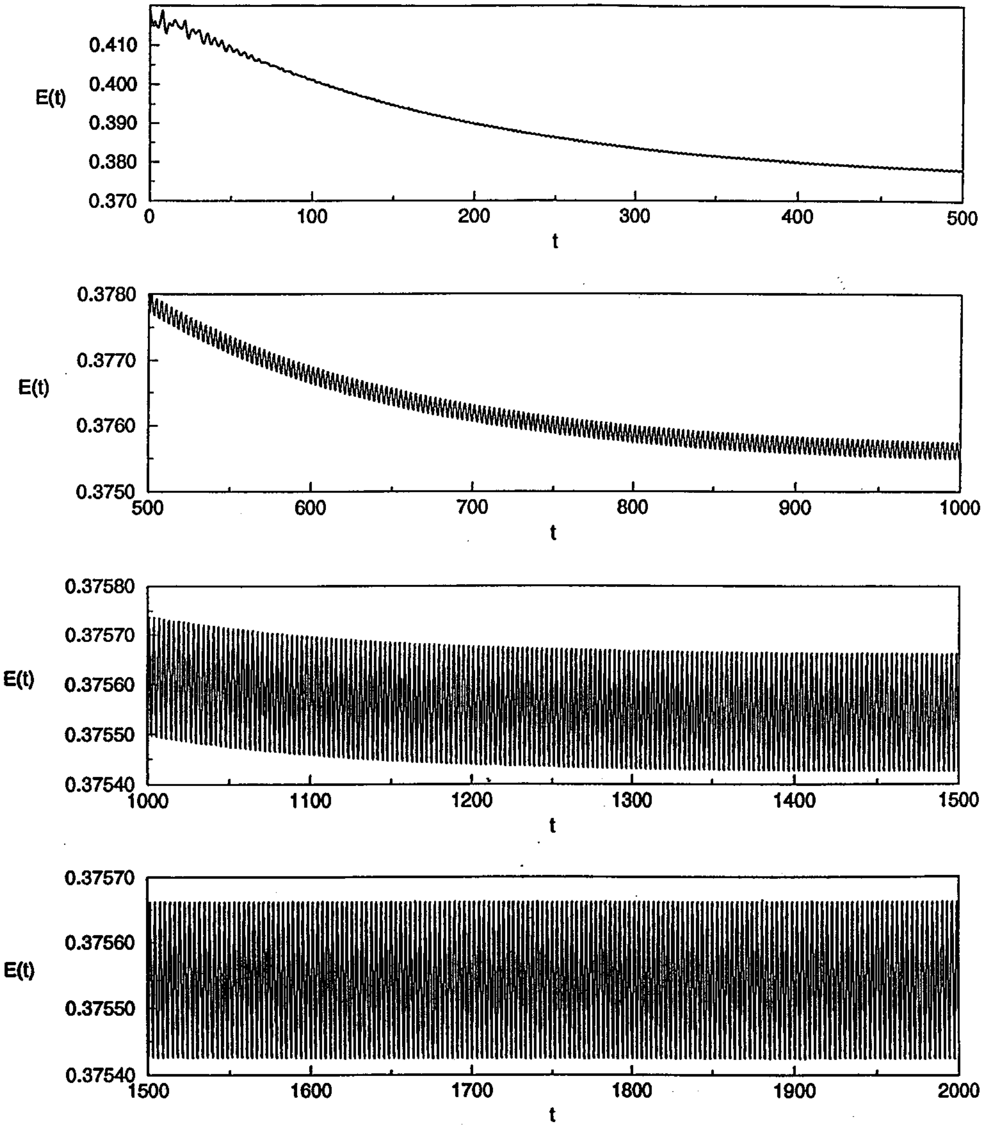

Figure 5. Convergence histories of the total kinetic energy $E(t)$ for the regularized driven cavity: unsteady flow at $Re = 10500$, $\Delta t = 0.005$, $N \times M = 48 \times 48$.

flows, comparisons have been carried out for $Re = 10500$, where the oscillatory motion of the flow is well established. The spatial resolution corresponds to the same one used by Shen, $N \times M = 48 \times 48$, with a time step $\Delta t = 0.005$.

The total kinetic energy $E(t)$:

$$E(t) = \left\{ \sum_{i=0}^{N} \sum_{j=0}^{M} [u(x_i, y_j, t)^2 + v(x_i, y_j, t)^2] \right\}^{1/2}$$

has been used for quantitative comparisons, as well as the value of the time period. The convergence histories of $E(t)$, $t = n\Delta t$, are presented in Figure 5. Starting from steady state solution obtained at $Re = 10000$, the solution reaches its asymptotic periodic state at about $t = 1500$, while Shen has observed it at about $t = 4500$. However, we note a good agreement on the final amplitude of oscillations and on the extremum values: the maximum value is $E(t)_{\max} = 0.375663$ and $E(t)_{\min} = 0.375426$ is the minimum value, while for Shen, these values are 0.37548 and 0.37525, respectively. The corresponding power spectrum analysis for the present solution is displayed in Figure 6, which shows clearly the monoperiodic nature of the flow with a frequency $f = 1/T = 0.328$, from about 160 complete cycles after the asymptotic state is fully established (see Figure 5, for $t \in [1500, 2000]$). Shen has reported $T = 12.12$ (probably $4T$), while in this paper, it corresponds to $T = 3.04875$. Recently, Batoul *et al.* [24] have obtained a value of $T = 3.03$ for $Re = 10300$, which confirms the correctness of our result.

We have displayed a series of seven instantaneous iso-streamfunction contours for one complete cycle (Figure 7). All the features shown by Shen are well represented. As observed by Shen, persistent oscillations develop at secondary and tertiary vortices, particularly the appearance and the disappearance of the two tertiary vortices at the bottom and top right side.

### 4.3. *The rotating cavity with superimposed radial throughflow*

The configuration corresponds to a rotating annulus, where the flow enters radially at the inner radius, $a$, and exits the outer radius, $b$, between two co-rotating discs distant of $s$. The validation is carried out by comparisons of the computed results with theoretical solutions of Hide [32], experimental data of Owen and Pincombe [33] and numerical results of Maubert *et al.* [34]. Equivalent Dirichlet boundary conditions to those used in Maubert *et al.* are imposed at the entrance and the exit for the velocity.

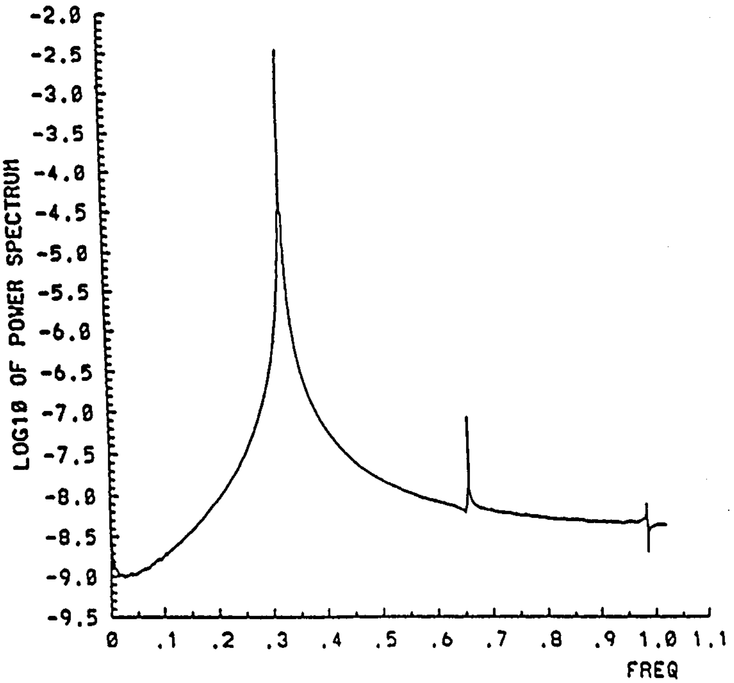

Figure 6. Power spectrum analysis of the total kinetic energy $E(t)$ for the regularized driven cavity: unsteady flow at $Re = 10500$, $\Delta t = 0.005$, $N \times M = 48 \times 48$.

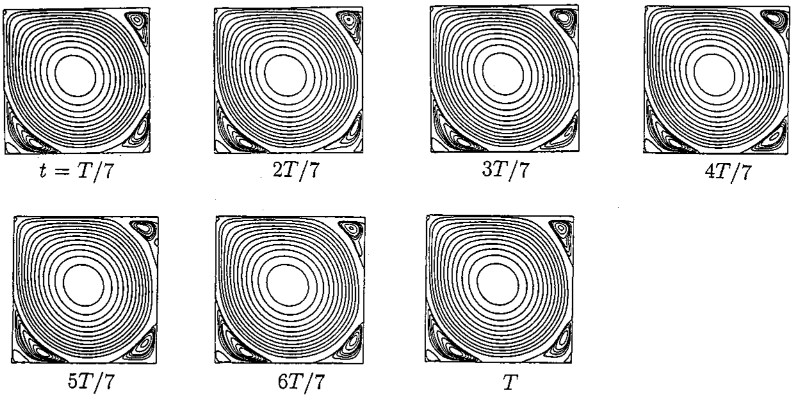
$t = T/7$ $2T/7$ $3T/7$ $4T/7$

$5T/7$ $6T/7$ $T$

Figure 7. Temporal evolution of instantaneous iso-streamfunction contours for the regularized driven cavity: unsteady flow at $Re = 10500$, $\Delta t = 0.005$, $N \times M = 48 \times 48$.

The geometry of the cavity is defined by an aspect ratio $A = (b - a)/s = 3.37$ and a curvature parameter $R_c = (b + a)/(b - a) = 1.22$, corresponding to the one studied experimentally by Owen and Pincombe [33]. Maubert *et al.* found a steady state solution at the value of the rotational Reynolds number $Re_\phi = \omega b^2/\nu = 25000$ for values of the dimensionless mass flow rate $C_w = Q/\nu b \leq 100$. For higher values of $C_w$, the flow evolves into a chaotic temporal behavior through several bifurcations (see also Reference [36]). In the present study, steady state solution at $C_w = 100$ and $Re_\phi = 25000$, corresponding to 'non-linear' Ekman layer flow regime, is reported. Computations have been achieved with the same spatial resolution used in Maubert *et al.*, $N \times M = 40 \times 40$.

The flow structure is displayed in Figure 8. All the features mentioned in the literature for the set of parameters values considered are well represented by the solution. The four distinct regions described by Hide [32], observed experimentally by Owen and Pincombe [33] and obtained numerically by Maubert *et al.* [34] are shown: the source (inlet) region, the separate Ekman layers along the rotating discs, the sink (outlet) region and the inviscid core. The flow exhibits a symmetry with respect to the midhorizontal plane. The radial length of the inlet region is larger than that of the outlet region, which is characteristic of non-linear regime. Indeed, Hide has mentioned the importance of the inertial terms in these regions.

Comparisons have been carried out for the radial length of the inner layer and for the axial variations of the radial and azimuthal velocity components. The radial length is computed as being the distance from the entrance to the location where the source region moves into the

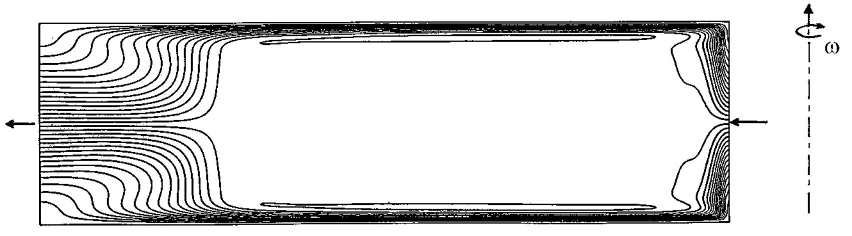

Figure 8. Streamlines for the rotating cavity with superimposed radial throughflow: $Re_\phi = 25000$, $C_\omega = 100$, $A = 3.37$, $R_c = 1.22$, $N \times M = 40 \times 40$.

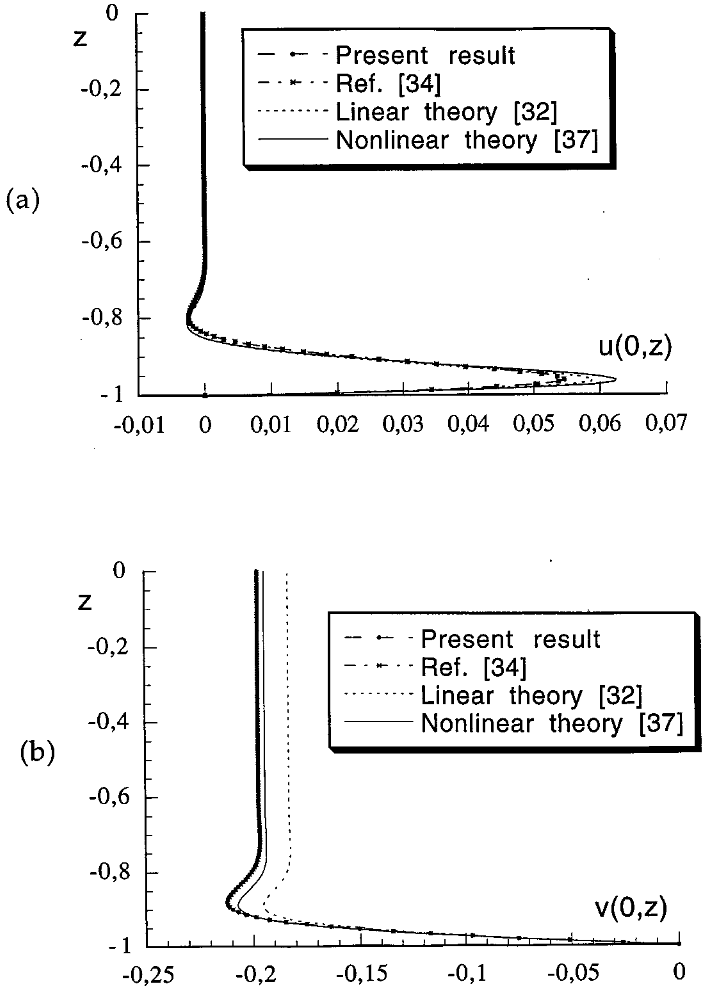

Figure 9. Axial variations of (a) the radial velocity component $u/\omega b$ and (b) the azimuthal velocity component $v/\omega b$ at midradial section for the rotating cavity. Comparison with available solutions for $Re_\phi = 25000$, $C_\omega = 100$, $A = 3.37$, $R_c = 1.22$, $N \times M = 40 \times 40$.

Ekman layers. From the streamlines displayed in Figure 8, we obtained $\Delta E/a = 2.374$. The theoretical estimate of Hide gives $\Delta E/a = 2.3747$ with his linear analysis, while the empirical correlation found by Owen and Pincombe gives $\Delta E/a = 2.375$. There is good qualitative agreement between the computed solution and the theoretical and experimental values. This confirms the correctness of the representation of the flow structure obtained with the present method.

The velocity profiles $u$ and $v$ are displayed at the midradial section of the cavity, $r = 0$, and for half height $z \in [-1, 0]$, because of the symmetry of the flow (see Figure 8). Comparisons with the classical Ekman layer (linear) and an extension to non-linear flow regimes [37] solutions and with numerical profiles obtained by Maubert *et al.* are reported in Figure 9. For the axial variation of the radial velocity component, the two computed and the theoretical solutions exhibit the same characteristic behavior, with a weak reverse flow between the Ekman layer and the core region (Figure 9(a)), which is also visible on the flow structure

Table V. Comparison of the geostrophic velocity at midradial section of the rotating cavity: $Re_\phi = 25\,000$, $C_\omega = 100$, $A = 3.37$, $R_c = 1.22$, $N \times M = 40 \times 40$.

| Linear theory [32] | Non-linear theory [37] | Reference [36] | Present result |
|---|---|---|---|
| $-0.18317$ | $-0.1943$ | $-0.19733$ | $-0.19736$ |

reported above. The two computed profiles obtained with different approaches (coupled versus time splitting method) using both pseudospectral approximation are identical. For the axial profile of the azimuthal velocity, a good agreement is also obtained for all the solutions (Figure 9(b)). The geostrophic solution proposed by Faller [37], including non-linear effects, is closer to the computed ones, indicating the importance of inertial terms. The respective values of the geostrophic velocity are reported in Table V.

## 5. CONCLUSION

An improved projection scheme is presented and applied to spectral methods associated with a second-order multistep time scheme, for the resolution of the incompressible Navier–Stokes equations. The major goal of the method is to allow the treatment of problems involving time variations of the pressure gradient at boundaries. This is done by introducing a correct predictor for the pressure at each time step, derived directly from the Navier–Stokes equations, in the former algorithm proposed by Goda [16] and Gresho [17]. Moreover, it is shown that the present algorithm reduces the velocity slip, compared with the previous one. This easy-to-implement method does not exhibit any numerical divergence boundary layer, as the incompressibility constraint is satisfied exactly inside the interior domain. Also, it does not require the use of staggered grids. It has also been found that the numerical stability constraint is not very restrictive, and computational costs as well as memory requirements remain inside a reasonable range. Very good agreement is obtained from comparison of the results with available solutions, for the prediction of different flow regimes (steady and unsteady) in the regularized driven cavity configuration and of the non-linear Ekman flow regime in the rotating cavity submitted to radial throughflow. The Ekman boundary layers structure accompanied by the presence of a fine recirculation layer, observed in experiments and described by theory, is a severe test problem to validate the present pseudospectral method. An extension of the code to the study of the fully three-dimensional regimes is in progress for the latter application.

### ACKNOWLEDGMENTS

Computations were performed on CRAY YMP-2E (Computing Center of IMT, Château-Gombert, Marseille, France) and CRAY-C98 (IDRIS, Orsay, France) with support of 'Conseil Régional PACA' and of CNRS. Financial support from DRET (group 6) is also gratefully acknowledged. The authors acknowledge Pr R.L. Sani (University of Colorado, Boulder, CO, USA) and Dr R. Peyret (Université de Nice, France) for their helpful assistance throughout the course of this work, and also Dr P. Bontoux (IRPHE, Marseille, France), Dr J. Ouazzani (ARCOFLUID, Aix-en-Provence, France) and Dr I. Raspo (IRPHE, Marseille, France) for fruitful discussions.

## REFERENCES

1. D. Gottlieb and S.A. Orszag, 'Numerical analysis of spectral methods: Theory and Applications', *CBMS Regional Conf. Series in Appl. Math.*, *SIAM*, 1977.
2. C. Canuto, M.Y. Hussaini, A. Quarteroni and T.A. Zang, *Spectral Methods in Fluid Dynamics*, Springer, Berlin, 1987.
3. L.S. Tuckerman, 'Divergence-free velocity fields in nonperiodic geometries', *J. Comput. Phys.*, **80**, 403–441 (1989).
4. A.K. Wong and J. Reizes, 'The vector potential in the numerical solution of the three-dimensional fluid dynamics problems in multiply connected regions', *J. Comput. Phys.*, **62**, 124–142 (1986).
5. A. Randriamampianina, 'On the use of vorticity vector-potential with a spectral tau method in rotating annular domains', *Finite Elem. Anal. Des.*, **16**, 299–307 (1994).
6. A.J. Chorin, 'A numerical method for solving incompressible viscous flow problems', *J. Comput. Phys.*, **2**, 12–26 (1967).
7. R. Peyret and T.D. Taylor, *Computational Methods for Fluid Flow*, Springer, Berlin, 1983.
8. L. Kleiser and U. Schumann, 'Treatment of incompressibility and boundary conditions in 3-D numerical spectral simulations of plane channel flows', in E.H. Hirschel (ed.), *Proc. 3rd GAMM Conf. on Numerical Methods in Fluid Mechanics*, Vieweg, Braunschweig, 1980, pp. 165–173.
9. A.J. Chorin, 'Numerical simulation of the Navier–Stokes equations', *Math. Comput.*, **22**, 745–762 (1968).
10. R. Temam, 'Une méthode d'approximation de la solution des équations de Navier–Stokes', *Bull. Soc. Math. France*, **98**, 115–152 (1968).
11. R.I. Issa, 'Solution of the implicitly discretized fluid flow equations by operator splitting', *J. Comput. Phys.*, **62**, 40–65 (1986).
12. J. Kim and P. Moin, 'Application of a fractional-step method to incompressible Navier–Stokes equations', *J. Comput. Phys.*, **59**, 308–323 (1985).
13. P. Gresho and R.L. Sani, 'On pressure boundary conditions for the incompressible Navier–Stokes equations', *Int. j. numer. methods fluids*, **7**, 1111–1145 (1987).
14. L.J.P. Timmermans, P.D. Minev and F.N. van de Vosse, 'An approximate projection scheme for incompressible flow using spectral elements' *Int. j. numer. methods fluids*, **22**, 673–688 (1996).
15. H.C. Ku, T.D. Taylor and R.S. Hirsh, 'Pseudospectral methods for solution of the incompressible Navier–Stokes equations', *Comput. Fluids*, **15**, 195–214 (1987).
16. K. Goda, 'A multistep technique with implicit difference schemes for calculating two- and three-dimensional cavity flows', *J. Comput. Phys.*, **30**, 76–95 (1979).
17. P. Gresho, 'On the theory of semi-implicit projection methods for viscous incompressible flow and its implementation via a finite element method that also introduces a nearly consistent mass matrix. Part 1: Theory', *Int. j. numer. methods fluids*, **11**, 587–620 (1990).
18. J. Van Kan, 'A second-order accurate pressure-correction scheme for viscous incompressible flow', *SIAM J. Sci. Stat. Comput.*, **7**, 870– 891 (1986).
19. S.A. Orszag and L. Kells, 'Transition to turbulence in plane Poiseuille and Couette flow', *J. Fluid Mech.*, **96**, 159–205 (1980).
20. S.A. Orszag, M. Israeli and M. Deville, 'Boundary conditions for incompressible flows', *J. Sci. Comput.*, **1**, 75–111 (1986).
21. G.E Karniadakis, M. Israeli and S.A. Orszag, 'High-order splitting methods for the incompressible Navier–Stokes equations', *J. Comput. Phys.*, **97**, 414–443 (1991).
22. J. Shen, 'Hopf bifurcation of the unsteady regularized driven cavity flow', *J. Comput. Phys.*, **95**, 228–245 (1991).
23. O. Botella, 'On the solution of the Navier–Stokes equations using Chebyshev projection schemes with third-order accuracy in time', *Comput. Fluids*, **26**, 107–116 (1997).
24. A. Batoul, H. Khallouf and G. Labrosse, 'Une méthode de résolution directe (pseudo-spectrale) du problème de Stokes 2D/3D instationnaire. Application à la cavité entraînée carrée', *C. R. Acad. Sci.*, *Paris*, *Serie II*, **319**, 1455–1461 (1994).
25. J.M. Vanel, R. Peyret and P. Bontoux, 'A pseudospectral solution of vorticity-streamfunction equations using the influence matrix technique', in K.W. Morton and M.J. Baines (eds.), *Numerical Methods Fluid Dynamics II*, Clarendon, Oxford, 1986, pp. 463–475.
26. C.W. Gear, 'Numerical initial value problems in ordinary differential equations', in G.E. Forsythe (ed.), *Automatic Computation*, Prentice Hall Englewood Cliffs, NJ, 1971.
27. D.B. Haidvogel and T.A. Zang, 'The accurate solution of Poisson's equation by expansion in Chebyshev polynomials', *J. Comput. Phys.*, **30**, 167–180 (1979).
28. P. Haldenwang, G. Labrosse, S. Abboudi and M. Deville, 'Chebyshev 3-D spectral and 2-D pseudospectral solvers for the Helmholtz equation', *J. Comput. Phys.*, **55**, 115–128 (1984).
29. U. Ehrenstein, 'Méthodes spectrales de résolution des équations de Navier–Stokes: Application à des écoulements de convection double-diffusive', *Doctorate Thesis*, Université de Nice, France, 1986.
30. U. Ehrenstein and R. Peyret, 'A Chebyshev collocation method for the Navier–Stokes equations with application to double-diffusive convection', *Int. j. numer. methods fluids*, **9**, 427–452 (1989).
31. Y. Morchoisne, 'Inhomogeneous flow calculations by spectral methods: monodomain and multi-domain techniques', in G. Voigt, D. Gottlieb and Y. Hussaini (eds.), *Proc. Symposium Spectral Methods for Partial Differential Equations*, *SIAM-CBMS*, 1984, pp. 181–208.

32. R. Hide, ‘On source-sink flows in rotating fluids’, *J. Fluid Mech.*, **32**, 737–764 (1968).
33. J.M. Owen and J.R. Pincombe, ‘Velocity measurements inside a rotating cavity with a radial outflow of fluid’, *J. Fluid Mech.*, **99**, 111–127 (1980).
34. P. Maubert, A. Chaouche, E. Crespo del Arco and P. Bontoux, ‘Régimes d’écoulement instationnaires dans une cavité annulaire tournante soumise à un flux radial forcé’, *C. R. Acad. Sci.*, *Paris*, *Serie II*, **315**, 1593–1600 (1992).
35. A.M. Chaouche, A. Randriamampianina and P. Bontoux, ‘A collocation method based on an influence matrix technique for axisymmetric flows in an annulus’, *Comp. Meth. Appl. Mech. Eng.*, **80**, 237–244 (1990).
36. E. Crespo del Arco, P. Maubert, A. Randriamampianina and P. Bontoux, ‘Spatio-temporal behaviour in a rotating annulus with a source-sink flow’, *J. Fluid Mech.*, **328**, 271–296 (1996).
37. A.J. Faller, ‘A experimental study of the instability of the laminar Ekman boundary layer’, *J. Fluid Mech.*, **15**, 560–576 (1963).